國立台灣大學工學院化學工程學系

碩士論文

Department of Chemical Engineer

College of Engineering

National Taiwan University

Master Thesis

水在磷烯奈米通道的毛細作用：表面結構的影響

Water Wicking in 2-dimensional Phosphorene Nanochannel: Effect of Surface Texture

黃千又

Chien-Yu Huang

指導教授：諶玉真 博士

Advisor：Yu-Jane Sheng, Ph.D.

中華民國 112 年 6 月

June, 2023

doi:10.6342/NTU202301104

國立臺灣大學碩(博)士學位論文
口試委員會審定書

水在磷烯奈米通道的毛細作用：表面結構的影響
Water wicking in 2-dimensional phosphorene nanochannel : effect of surface texture

本論文係黃千又(R10524029)在國立臺灣大學化學工程學系、所完成之碩(博)士學位論文，於民國 112 年 06 月 15 日承下列考試委員審查通過及口試及格，特此證明

口試委員：

謝 子 真 (簽名)

(指導教授)

曹恒光

黃俊仁

孫仲勳

系主任、所長 廖英志 (簽名)

(是否須簽章依各院系所規定)

誌謝

非常感謝指導老師 諶玉真教授以及曹恆光教授在整個研究過程中的細心指導與支持。從碩士班一年級開始到現在，老師們一直以來都對我的研究給予很大的幫助。在研究過程中，無論我遇到什麼樣的困難，您們總是願意花時間聆聽我的問題，給予我許多專業建議與指導。另外，我還對老師們對實驗的嚴謹與執著態度感到印象深刻，這樣的榜樣激勵我不斷努力學習與成長。這兩年的日子，真的非常謝謝兩位老師的指導，我以最誠摯的心表達我的感激之情。

在學校實驗室中，能夠與優秀的學長姊、同儕以及學弟妹一起努力與切磋，是一件難得可貴的經驗。這樣的學習環境讓我能與志同道合的人互相學習與交流，共同成長茁壯。首先，感謝心瑀、昱浩、明璋和昕緯時常給予我研究上的指導與建議，你們的幫助讓我能更快地熟悉模擬實驗的內容，進一步提升我的研究能力。同時，我也要感謝庭瑜和冠臨，在學習的道路上有你們的陪伴，讓我感到不孤獨與寂寞，你們的支持讓我以更好的狀態應對課業上的挑戰。最後也謝謝實驗室的學弟妹這段時間的熱心協助，為我研究生活增添快樂的回憶！感謝大家陪我一起走過這兩年，即使我們即將各奔東西，但祝福你們往後能突破自己和抓住成功！

同時，我要特別感謝我最親愛的家人，因為有您們一路的付出與鼓勵，我才能夠無後顧之憂地專注在學業上，努力追求目標。無論是陪伴我度過學業中的艱難時刻，還是在我取得成就時分享喜悅，您們始終是我最堅強的後盾。我感謝您們對我的無私奉獻和信任，我會繼續努力，以回報你們對我的愛與支持。即使離開學校，我也會在不同領域努力朝目標前進，不忘您們對我的教誨。謝謝你們一直以來的陪伴與支持！

最後，謹向所有幫助我、關心我的人致上滿滿的謝意，並將這份成果呈現給你們！

doi:10.6342/NTU202301104

摘要

我們將運用分子動力學方法，探索水在由二維磷烯製成的納米通道中的毛細動力學行為。首先，我們研究在奈米尺度下水滴在磷烯薄片上的部分濕潤行為，發現水滴在開始潤濕後，其潤濕面積(A)和內能(ΔE)遵循冪定律，潤濕面積與時間的二分之一次方成正比，內能則與時間的負二分之一次方成正比。此外，在受限奈米管道內的水栓模擬中測量拉普拉斯壓力(Laplace pressure)和平衡接觸角(equilibrium contact angle)，確認楊-拉普拉斯方程(Young-Laplace equation)在納米尺度上的適用性。在毛細管模擬實驗中，對於寬度為多層(N)磷烯薄片的通道中，觀察水自發得浸潤行為，並發現滲透長度和內能變化都與時間的二分之一次方成正比。然而，在狹窄的奈米通道(N＝2～5)中，滲透速率取決於管壁的表面結構(拱橋狀和鋸齒狀)。隨著板寬增加，這種影響效應逐漸減弱。我們觀察到除了 N＝1 之外，隨著板寬寬度增加，滲透速率隨之下降，這與 Washburn’s equation 預測方向相互矛盾。與由光滑的石墨烯製作而成的奈米通道相比，磷烯基通道的滲透速率較低。但是，隨著通道寬度增加，這種差異逐漸減小，這結果表示表面粗糙度對於較大的通道寬度影響變得不那麼顯著。

doi:10.6342/NTU202301104

Abstract

The imbibition dynamics of water in a nanochannel made of the two-dimensional phosphorene is explored using Molecular Dynamics. The partial wetting behavior of water nanodroplets on phosphorene sheets is examined first. The initial spreading of the wetted area (A) and internal energy (ΔE) are found to follow the power law, $A \sim t^{1/2}$ and $\Delta E \sim -t^{1/2}$. Additionally, the Laplace pressure and equilibrium contact angle, determined from water plugs confined within nanoslits, verify the applicability of the Young-Laplace equation at the nanoscale. For water wicking in channels with a width of N layers of phosphorene sheets, the rate of change of both the penetration length and internal energy is proportional to $t^{1/2}$. However, the imbibition rate in narrow nanoslits (N = 2 ~ 5) depends on the orientation (armchair and zigzag) of walls. This effect gradually diminishes as N increases. It was observed that, except for N = 1, the imbibition rate decreases with increasing channel width, which contradicts the prediction of Washburn's equation. Compared to smooth graphene-based channels, the imbibition rate is lower in phosphorene-based channels. Nonetheless, this difference decreases as the channel width increases, suggesting that the impact of surface roughness becomes less pronounced with larger channel widths.

KEYWORDS: *capillary flow, phosphorene nanochannels, imbibition dynamics, spreading dynamic, roughness*

doi:10.6342/NTU202301104

Content

doi:10.6342/NTU202301104

List of Figures

doi:10.6342/NTU202301104

doi:10.6342/NTU202301104

Nomenclature

A	wetted area	Greek symbols	
a	internal distance	α	slope of the imbibition flow
ΔE	internal energy difference	γ_{sl}	surface tension
ΔF	free energy difference	ρ	liquid density
L	capillary channel height	μ	viscosity
l	penetration length	τ	inertial time
N	number of phosphorene sheets	θ_D	dynamic contact angle
ΔP	Laplace pressure	θ_c	equilibrium contact angle
Q	flow rate		
R	radius of the spherical droplet		
R_1,R_2	principal radii of curvature	Subscripts	
r	radius	l	liquid
t	time	v	vapor
v_z	imbibition velocity	s	solid
w	channel width	x, y, z	coordinate

doi:10.6342/NTU202301104

1. Introduction

Capillary flow is a phenomenon in which a liquid is spontaneously absorbed into a narrow space due to wetting. It plays a role in various natural activities [1-4], including water uptake by plants, as well as industrial processes [5-8] such as oil recovery and water separation. The process of capillary imbibition is influenced by factors such as the viscosity of the liquid (μ), the geometry of the capillaries, and the solid-liquid interactions [9]. The classic description of dynamics of capillary flow in small channels are often described by Washburn's equation [10-12]. The driving capillary force in Washburn's equation is the pressure drop across a curved liquid surface, which is proportional to the product of the mean curvature of the meniscus and the surface tension (γ_{lg}) of the liquid, as described by the Young-Laplace equation [13, 14]. The no-slip boundary condition is commonly adopted, and it has been observed that the penetration length (l), defined as the distance from the reservoir to the meniscus, is proportional to the square root of the imbibition time [15, 16]. In a slit with the channel width (w), the constant of proportionality is the square root of $\gamma_{lg}\cos(\theta_D)\,w/3\mu$. Here θ_D denotes the dynamic contact angle, which is generally greater than the equilibrium contact angle between the liquid and the channel surface [17].

In recent years, nanofluidics has emerged as an exciting field of exploration due to advances in nanofabrication techniques that enable the creation of individual artificial channels with nanometer-scale dimensions [18-21]. Graphene-based nanochannels are often fabricated due to their unique and tunable properties [22], and they remain stable and reusable after the transport of water and ions [23-25]. The study of these channels has led to the discovery of many unexpected behaviors and properties. The capillary flow of water in graphene nanoslits was investigated for different channel widths, ranging from 0.7 to tens of nanometers, and the unexpectedly fast flow velocity of up to 1 m/s was

doi:10.6342/NTU202301104

reported [24, 26-28]. Additionally, the rate of water transport changes non-monotonically with the width of graphene nanoslits, which contradicts the qualitative prediction of Washburn's equation [28]. Molecular dynamics simulations have also shown that the transport properties of water, such as shear viscosity and diffusivity, are significantly influenced by the channel width, especially in the region of 6.8 to 7.8 Å [29].

Alongside smooth graphene nanomaterials, a new two-dimensional (2D) layered material called black phosphorus (BP), consisting of multiple layers of phosphorene, has gained attention for its potential applications [30-34]. The atomic layers of phosphorene within BP have a puckered structure and are held together by van der Waals interactions. Phosphorene consists of phosphorus atoms, each with covalent bonds to three adjacent phosphorus atoms [35-37]. BP displays anisotropic electronic and optical properties due to its puckered honeycomb structure, setting it apart from other 2D materials [38, 39]. Phosphorene nanosheets can be fabricated by the top-down methods, such as liquid-based exfoliation, mechanical exfoliation, and electrochemical exfoliation [40-45], and they are stable when in contact with deaerated water [46, 47]. The wetting behavior of water nanodroplets on both pristine and strained phosphorene was studied by molecular dynamics (MD) simulations [48]. The contact angle on the pristine phosphorene is about 72° (weak hydrophobicity), while it increases on the strained phosphorene. The water angle grows monotonically with longitudinal strain but displays non-monotonic change with transverse strain. This study reveals that the anisotropic wetting behavior on the surface of phosphorene is enhanced when it is stretched longitudinally or transversely.

Due to its biocompatibility and in vivo biodegradability, BP is a suitable material for biomedical devices, including sensors and drug delivery systems [49]. Similar to graphene-based nanochannels, phosphorene-based nanochannels may be constructed for the transport of water and ions. The capillary flow of water in phosphorene nanoslits may

doi:10.6342/NTU202301104

differ significantly from that in graphene nanoslits due to differences in their surface structures. While the latter is molecularly smooth, the former has a relatively rough surface characterized by the armchair or zigzag orientation [50]. In this work, molecular dynamics (MD) simulations are employed to explore the wetting behavior of water droplets on phosphorene surfaces and the wicking dynamics of water in phosphorene-based nanochannels. The spreading dynamics of the water droplet is studied by tracking changes in the wetting area and internal energy over time. Moreover, the validity of the Young-Laplace equation is examined by considering water plugs confined within nanoslits. The wicking dynamics is investigated by monitoring the variation of the penetration length and internal energy with time. The influences of the width of the nanochannel and the orientation of the wall on the capillary flow are studied. Finally, the comparison of the wicking dynamics between phosphorene-based and graphene-based nanoslits is made.

2. Method

MD simulations were conducted using the Nanoscale Molecular Dynamics (NAMD) simulation package, while visualization and analysis were performed using Visual Molecular Dynamics (VMD) [51]. Compared to classical MD, NAMD is a parallel molecular dynamics code that utilizes efficient electrostatics evaluation and temperature and pressure controls [52, 53]. The TIP4P/2005 rigid water model is adopted to describe the water molecule [54] because it better depicts the hydrogen-bonding network, viscosity, and surface tension. The Lennard-Jones (L-J) 12-6 potential with a cutoff distance of 12 Å and the particle-mesh Ewald summation method for long-range electrostatic interactions are used. NAMD simulations were performed at 300 K in a canonical (NVT) ensemble with the Langevin thermostat. The calculated viscosity of water is $\mu = 0.855$

doi:10.6342/NTU202301104

mPa·s [55], which agrees with the experimental value of 0.853 mPa·s.

The phosphorene sheet serves as both the substrate for wetting and the channel wall for imbibition. **Figure 1(a)** shows the orthorhombic structure of phosphorene obtained via the space group Cmca [50]. The top view of a phosphorene sheet displays a honeycomb lattice structure similar to graphene. However, it exhibits an anisotropic arrangement along one basic vector. In phosphorene, the direction of periodic protrusion is commonly referred to as the "armchair" orientation, while the direction of the groove is known as the "zigzag" orientation. The initial configurations of phosphorene were created using Materials Studio 8.0, with an interlayer distance of 0.52 nm between two phosphorene sheets [36, 57, 58]. In phosphorene, the L-J parameters between phosphorus atoms was derived based on density functional theory with no partial charge [56]. Similar treatment was carried out for graphene as well [59, 60]. The interaction parameters between different atoms were determined using the Lorentz-Berthelot mixing rule. All the interaction parameters of water, phosphorene, and graphene are given in **Table 1**.

In this work, two kinds of simulations were considered: the wetting behavior of water droplets on phosphorene sheets and the imbibition dynamics of water in phosphorene nanoslits. For a water droplet deposited on a phosphorene surface, the spreading process was monitored, and the equilibrium contact angle was determined. Two different sizes of water droplets were considered: one containing 4050 water molecules and the other containing 6000 molecules. To ensure a spherical shape and minimize system free energy, both droplets were equilibrated at 300 K for over 6 ns. Subsequently, the water droplet was bought into contact with a surface composed of three layers of phosphorene. The change in internal energy was recorded until reaching the equilibrium state. After reaching equilibrium, in each frame of snapshots, the local contact angles of water droplet along the contact line were measured using SCA20 software. The wetted

doi:10.6342/NTU202301104

area of water spreading on the phosphorene surface was estimated using ImageJ software.

In addition to studying the sessile droplet, the wetting behavior was also observed in a nanoslit filled with a water plug. A water plug consisting of 1500 water molecules was created within a nanoslit. The system was then minimized for 5000 steps and equilibrated at 300 K for 2 ns to reach equilibrium. The internal energy and Laplace pressure were recorded during the simulation, and the wetted area was estimated from the snapshots using ImageJ software. The values of the internal energy and Laplace pressure were averaged over 5 ns to obtain more reliable results. The wall of the nanoslit was constructed using three layers of phosphorene-based sheets with dimensions of 4.0 nm in the y-direction and 20 nm in the z-direction. The periodic boundary condition was applied in both the y- and z-directions to simulate an effectively infinite system. The widths of the nanoslits were chosen to accommodate an integer number of phosphorene layers [28]. For example, N = 2 corresponds to a width of 2×0.52 nm = 1.04 nm.

The imbibition dynamics were investigated in a nanoslit when it was in contact with a water reservoir, as depicted in **Figure 1(b)**. The water reservoir was minimized for 5000 steps and subsequently equilibrated in the NVT ensemble at 300 K for over 5 ns prior to placing the phosphorene wall on top. Afterward, the capillary system was minimized for 5000 steps. The penetration length of the meniscus was then monitored before it reached the end of the channel. Both the meniscus in the capillary and the water reservoir were exposed to the vapor phase. The capillary channel height (L) along the z-direction was 20 nm and the width of the slits was equal to N×a nm, where N represents the number of phosphorene sheets and a = 0.52 nm is the thickness of a phosphorene sheet. The box size was set to 4.0 nm in the y-direction, and periodic boundary conditions were applied in all three directions. To avoid the capillary flow outside the capillary channel, two smooth and flat graphene baffle walls were placed at the top of the reservoir. All atoms of the

doi:10.6342/NTU202301104

phosphorene sheets and graphene baffle were fixed in space during simulations.

Table 1. Force field parameters of phosphorene, graphene, and water: (a) non-bonded parameters and (b) bonded parameters.

(b) bonded parameters			
Bond		K_b (kcal/mol)	b_0 (Å)
	Oxygen atom of water (O_w)-hydrogen atom of water (H_w)	450.000	0.9572
	phosphorus atom of one of the planes of Phosphorene structure (P_{P1})-phosphorus atom in the other planes (P_{P2})	205.368	2.2250
	P_{P1}-P_{P1}	205.368	2.2250
	P_{P2}-P_{P2}	205.368	2.2250
	Carbon atom of graphene (C_g)-carbon atom of graphene (C_g)	322.550	1.420
Angle		K_θ (kcal/mol)	θ_0 (degrees)
	H_w–O_w-H_w	55.00	104.52
	P_{P1}- P_{P1}- P_{P1}	56.21	96.40
	P_{P2}- P_{P2}- P_{P2}	56.21	96.40
	P_{P1}- P_{P1}- P_{P2}	56.21	102.10

doi:10.6342/NTU202301104

	P_{P1}- P_{P2}- P_{P2}	56.21	102.10	
	C_g-C_g-C_g	53.35	120.00	
Improper angle		K_φ (kcal/mol)	φ_0 (degrees)	
	C_g-C_g-C_g-C_g	15	0	
Dihedral angle		K_χ (kcal/mol)	n (multiplicity)	δ (degrees)
	C_g-C_g-C_g-C_g	3.15	2	180

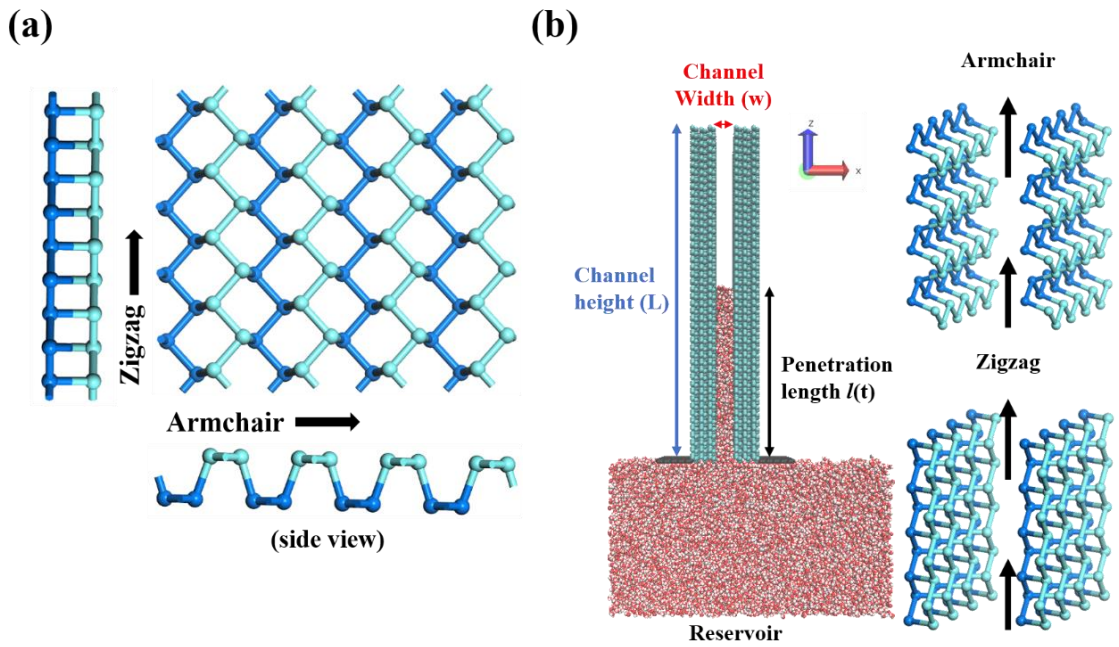

Figure 1. Schematic diagrams of (a) the phosphorene structure from top and side views, showing the armchair and zigzag orientations, and (b) the system configuration for capillary dynamics in a phosphorene nanoslit. The diagrams depicting the armchair and zigzag orientations of the channel walls are shown on the right side.

doi:10.6342/NTU202301104

3. Results

3.1 The wetting behavior of water on phosphorene surface

3.1.1 Spreading and equilibrium of a droplet on a surface

The imbibition of water into a phosphorene-based nanochannel is driven by interfacial tensions, which are reflected in the wetting behavior. To investigate the wetting behavior of water on the phosphorene surface, a water droplet containing 6000 water molecules was deposited onto a surface constructed by three layers of phosphorene sheets. Due to thermal fluctuations, the water droplet eventually comes into contact with the phosphorene surface when they are in close proximity to each other. Afterward, the water droplet started to spread outwards and wet the surface. The spreading process was observed and recorded through a series of snapshots from 0 to 6 ns, as shown in **Figure 2** (both side and top views). Over time, the height of the water droplet decreased while the wetted area increased. The water droplet reached equilibrium after 1.0 ns and the equilibrium contact angles along the armchair and zigzag directions were found to be $68.6° \pm 1.7°$ and $67.9° \pm 1.6°$, respectively, which are consistent with previously reported simulation data, 63.2°~72.0° [48, 61]. A similar result is also obtained for a smaller droplet with 4050 water molecules. Given the high equilibrium contact angle, the surface of phosphorene is considered to be relatively hydrophobic to a water droplet.

doi:10.6342/NTU202301104

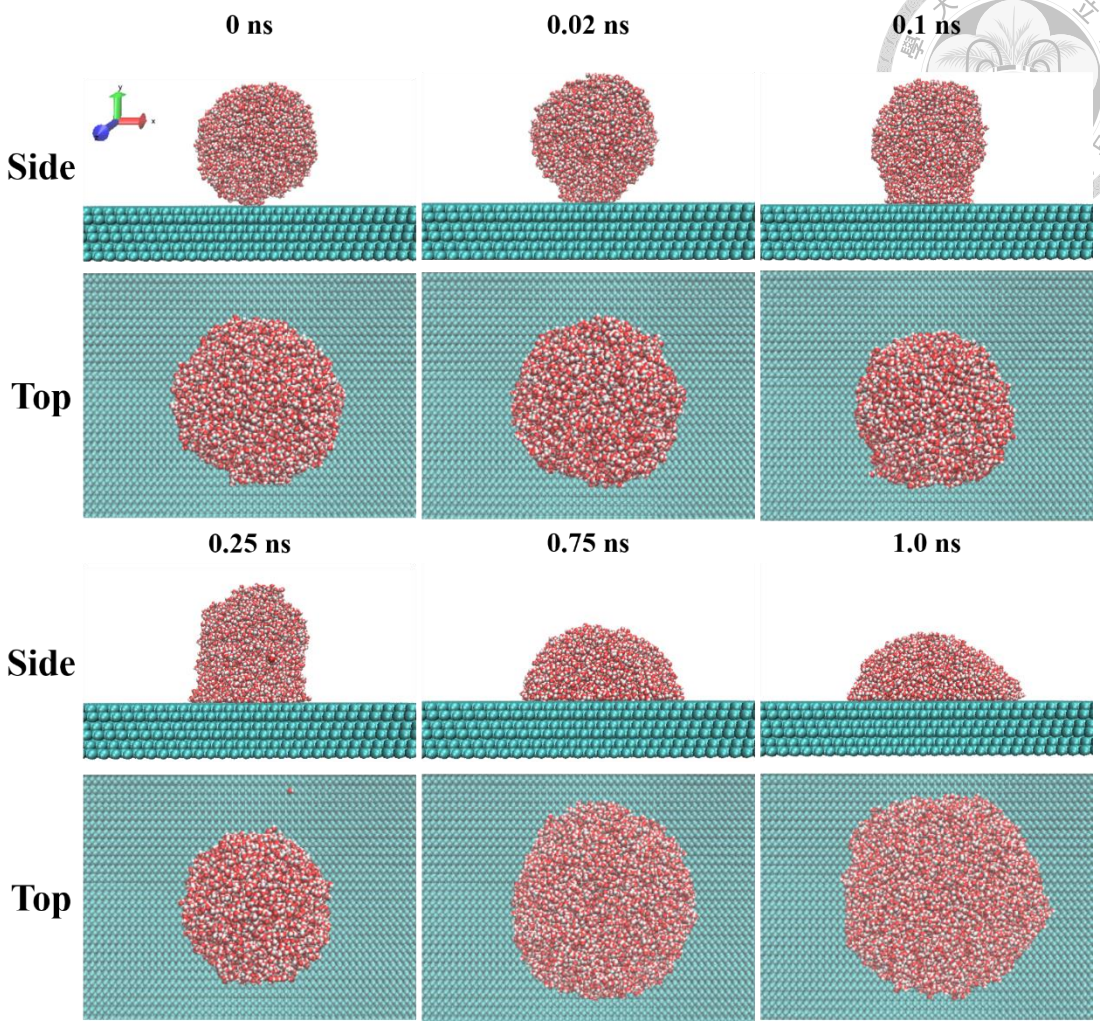

Figure 2. Snapshots (side and top views) of a water droplet deposited on the phosphorene surface at different time intervals.

When a droplet contacts a wettable surface, it tends to spread out in order to minimize the total surface free energy. This initial spreading process is usually rapid and governed by inertia rather than viscosity, as it is driven by the droplet's momentum [62]. The inertial time scale is expressed as $\tau = (\rho R^3/\gamma_{lv})^{1/2}$, where ρ represents the liquid density, R the radius of the spherical droplet, and γ_{lv} the vapor-liquid surface tension [62, 63]. For inertial spreading, the radius (r) of the wetted area (A) is expected to grow with the square root of time, $r \sim t^{1/2}$ or $A \sim t^1$ [64]. τ is estimated to be approximately 36 ps for the water droplet with radius of 4.4 nm. In contrast, viscous spreading eventually becomes

doi:10.6342/NTU202301104

dominant and it is generally described by Tanner's law, which follows the relation $r \sim t^{1/10}$ or $A \sim t^{1/5}$ for droplets with small contact angles [64-66]. **Figure 3(a)** displays how the wetted area changes over time for two droplets with different sizes. These data points are beyond the inertial spreading regime. The equilibration time is found to be about 0.75 and 0.95 ns for droplets containing 4050 and 6000 water molecules, respectively. Once equilibrium is reached, the wetted area of the sessile droplet remains constant, measuring 39.9 nm^2 and 56.5 nm^2 for the small and large droplets, respectively. The spreading dynamics were found to follow a power law approximation, $A \sim t^{1/2}$, which is inconsistent with either inertial spreading or Tanner's law. The exponent (1/2) is intermediate between that of inertial spreading (1) and Tanner's law (1/5). The spreading process is mainly governed by viscosity but its deviation from Tanner's law is probably due to a large contact angle and a finite time to reach equilibrium.

According to Young's equation, the equilibrium contact angle (θ_c) is related to the interfacial tensions through the equation, $\cos\theta_c = (\gamma_{sv} - \gamma_{sl})/\gamma_{lv}$ [67, 68], where γ_{sv} and γ_{sl} represent the solid-vapor and solid-liquid tensions, respectively. It is evident that $\gamma_{sl} - \gamma_{sv} < 0$, or $\gamma_{sl} < \gamma_{sv}$, due to the fact that $\cos\theta_c > 0$ or $\theta_c < 90°$. During the spreading process, the dominant contribution to the change in the system free energy (ΔF) is anticipated to arise from the solid-liquid contact area (i.e., the wetted area). The wetting process is accompanied by the decrease of the free energy. Therefore, one has $\Delta F(t) \sim (\gamma_{sl} - \gamma_{sv})A(t) < 0$ due to the gain of solid-liquid free energy and the loss of solid-vapor free energy. While determining the surface free energy through simulations is challenging, analyzing the change in internal energy (ΔE) resulting from wetting the surface can provide insight into the spreading process. After reaching equilibrium, the change in internal energy should become difficult to discern except for the influence of thermal fluctuations. Since the wetted area is proportional to the square root of time, it is expected that the decrease

doi:10.6342/NTU202301104

in internal energy will also follow a similar trend, that is, proportional to $t^{1/2}$. **Figure 3(b)** shows the plot of the change of internal energy against the square root of time for two different droplets, and the linear relationship is observed. The result suggests that the change in internal energy is primarily caused by the solid-liquid contact.

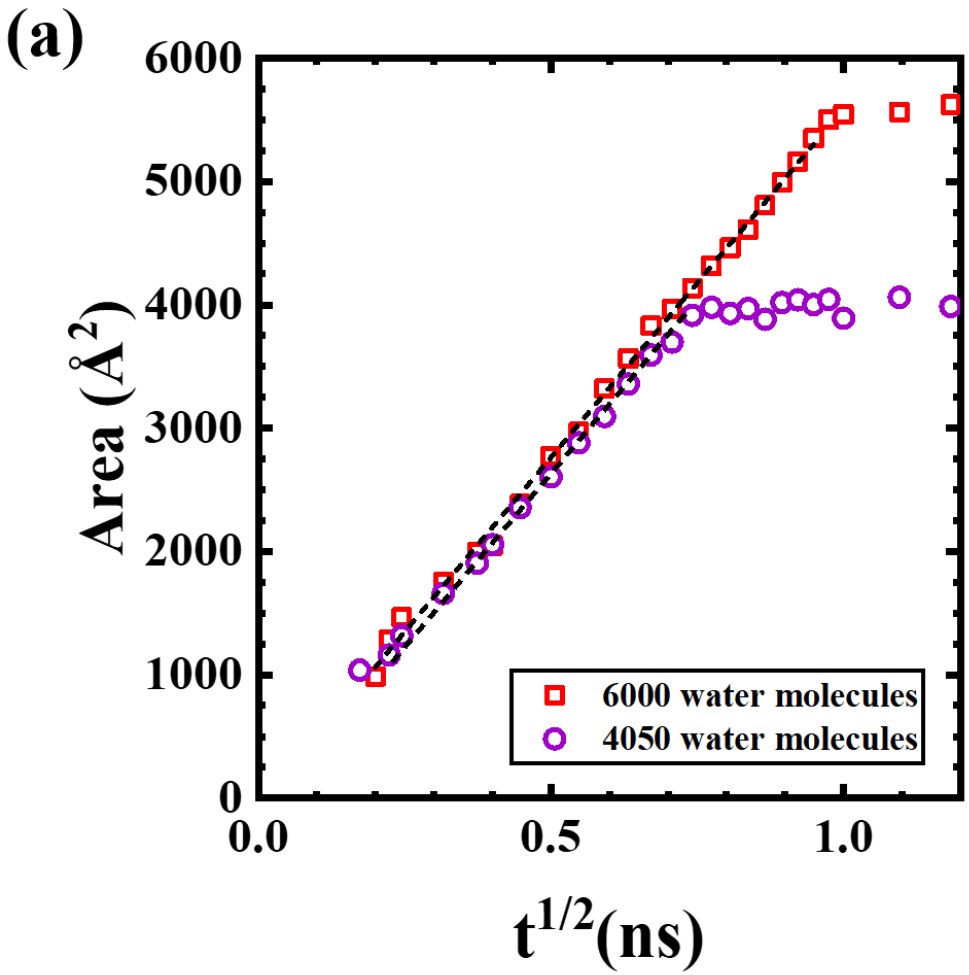

doi:10.6342/NTU202301104

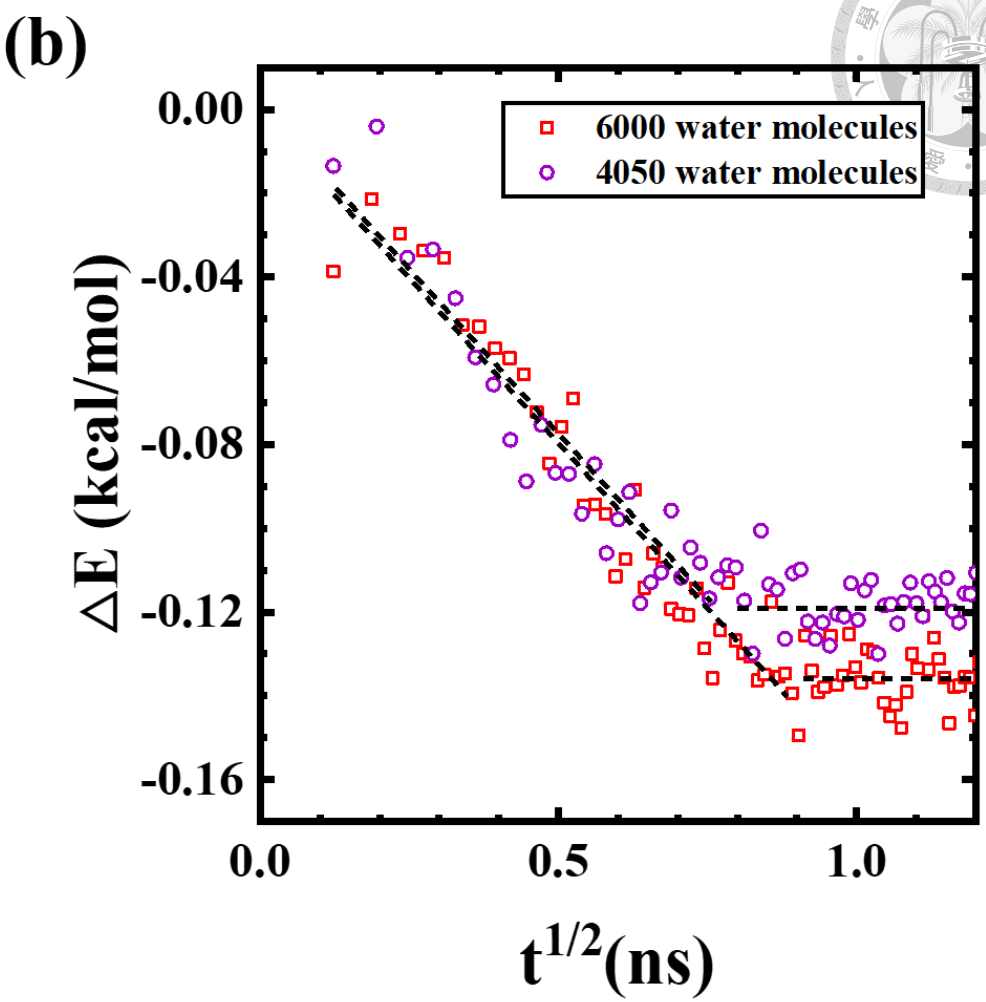

Figure 3. (a) The variation of wetted area (A) with the square root of time ($t^{1/2}$) and (b) the variation of internal energy (ΔE) with the square root of time ($t^{1/2}$) for two different sizes of water droplets

3.1.2 Water plug in a nanoslit and validity of Young-Laplace equation

In addition to the deposition of a water droplet on the surface of phosphorene, the wetting behavior can also be observed in a nanoslit filled with a water plug (2-dimensional droplet), as demonstrated in **Figure 4(a)**. The shape of the water plug, which contains 1500 water molecules, is dependent on the width of the nanoslit. The internal energy, wetted area, and pressure within the plug can be determined from simulations. Moreover, by analyzing the meniscus of the water plug, it is possible to evaluate both the

doi:10.6342/NTU202301104

equilibrium contact angle and Laplace pressure from Young-Laplace equation. The influence of the surface orientation (armchair and zigzag patterns) on the wetting properties is examined. The equilibrium contact angles determined from the water plug at different channel widths and surface orientations are approximately the same, around 70°. This value is slightly larger than the contact angle observed in the sessile droplet. **Figure 4(a)** displays the relationship between the change in internal energy (ΔE) and the channel width (w). $\Delta E(N)$ is defined as $E(w = Na) - E(w = a)$ and w ranges from N = 2 to N = 7. The equilibrium internal energy of the water plug along both the armchair and zigzag directions is calculated. It is found that the internal energy increase with increasing N, and this consequence is attributed to the decrease in the wetted area of the water plug, as depicted in the left inset. Based on the variation of internal energy with the wetted area (right inset), the equilibrium result of water plug is consistent with the non-equilibrium spreading process of the deposited droplet. Comparing the results along the armchair and zigzag directions, we found that the surface orientations have a negligible effect on the equilibrium wetting properties.

The Young-Laplace (Y-L) equation describes the relationship between the curvature of a liquid interface and the pressure difference (ΔP) across the interface of two fluids. In general, the Y-L equation can be expressed as $\Delta P = \gamma_{lv}(1/R_1 + 1/R_2)$, where R_1 and R_2 are the principal radii of curvature of the meniscus at the liquid-vapor interface [13, 69-71]. In the case of a water plug, the Laplace pressure is given by $\Delta P = \gamma_{lv}/R$. The radius of curvature of the meniscus is related to half of the slit width, $R = w/[2\cos(\theta_c)]$, where θ_c is the equilibrium contact angle. As a result, the Laplace pressure is inversely proportional to the channel width by $\Delta P = 2\gamma_{lv}\cos(\theta_c)/w$ based on the Y-L equation. **Figure 4(b)** shows the pressure difference as a function of the inverse of the channel width (1/N) for both the armchair and zigzag orientations in the phosphorene nanoslits. As N decreases from 7 to

doi:10.6342/NTU202301104

2, the Laplace pressure increases from 100 to 600 bar. These values are significantly greater than the atmospheric pressure (1 bar). It can be attributed to the strong influence of solid-liquid interactions resulting from the confinement of water within narrow phosphorene slits, known as the disjoining pressure [24].

It is evident that the variation of ΔP with 1/N can be well described by a linear line. According to the Y-L equation, the slope for the armchair and zigzag orientations is $2\gamma_{lv}\cos(\theta_c)/a$, with values of 877.4 and 824.2, respectively. Thus, the equilibrium contact angles associated with the armchair and zigzag orientations are obtained as 70.0° and 71.1°, respectively. These results determined from the Y-L equation are in an agreement with the direct measurements from the water plug, where the contact angles are approximately 69.8° and 70.0° for the armchair and zigzag orientations, respectively. This consistency demonstrates that the validity of the Y-L equation extends to nanoscale channels. In addition, water exhibits similar equilibrium wetting behavior on both the armchair and zigzag orientations of phosphorene.

doi:10.6342/NTU202301104

(a)

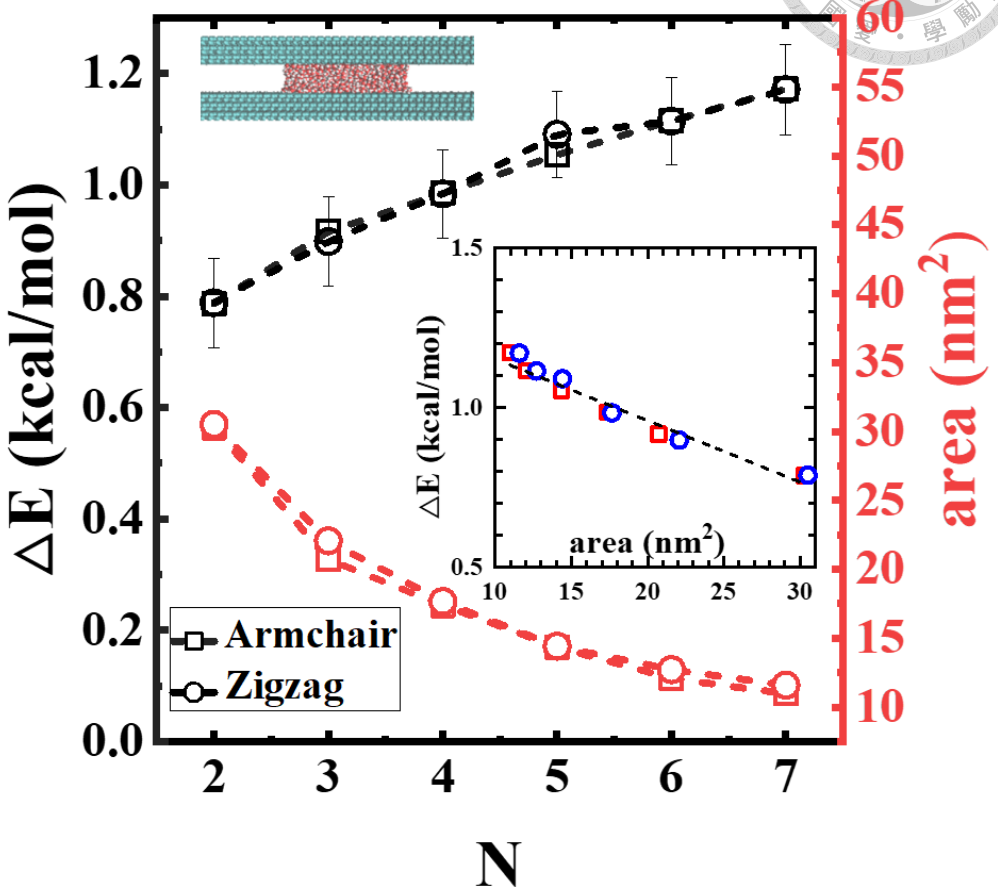

doi:10.6342/NTU202301104

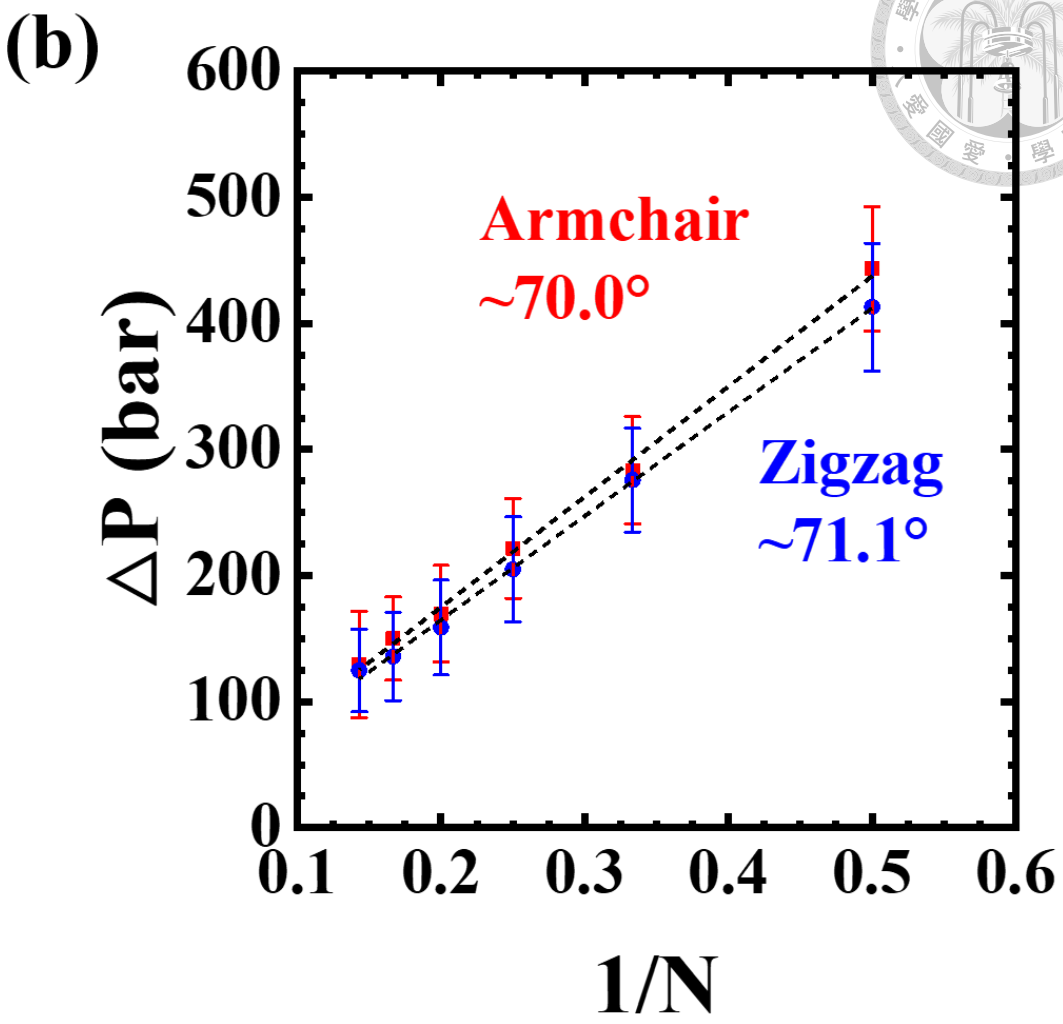

Figure 4. (a) The variation of the change in internal energy (ΔE) and wetted area (A) with the channel width (w=Na) of the phosphorene nanoslit. The image of the water plug (N = 3) and the plot of ΔE against wetted area are shown in the inset. (b) The variation of the Laplace pressure (ΔP) with the inverse of the channel width (1/N) for both armchair and zigzag orientations.

3.2 Imbibition dynamics: effect of armchair and zigzag orientations of the wall

The spontaneous capillary flow of water in the phosphorene-based nanochannel is observed and the imbibition dynamics can be quantitatively studied by monitoring the penetration length *l*(t). **Figure 5** shows a representative imbibition process of water in a

doi:10.6342/NTU202301104

phosphorene nanoslit with N = 4. When the nanoslit is placed on top of the water reservoir at t = 0 ns, capillary flow occurs spontaneously, and the meniscus advances forward, eventually reaching the end of the slit at around t = 27 ns. During the wicking process, the penetration length increases and is recorded, but it ceases to change once the meniscus reaches the end of the 20 nm channel. Although the accurate measurement of the meniscus in the channel is challenging due to thermal fluctuations, we found that the dynamic contact angles during imbibition were approximately 74.2° ± 2.8° at the position z = 12 nm. Consistent with expectations, the dynamic contact angle is found to be slightly larger than the equilibrium contact angle owing to the dynamic pressure.

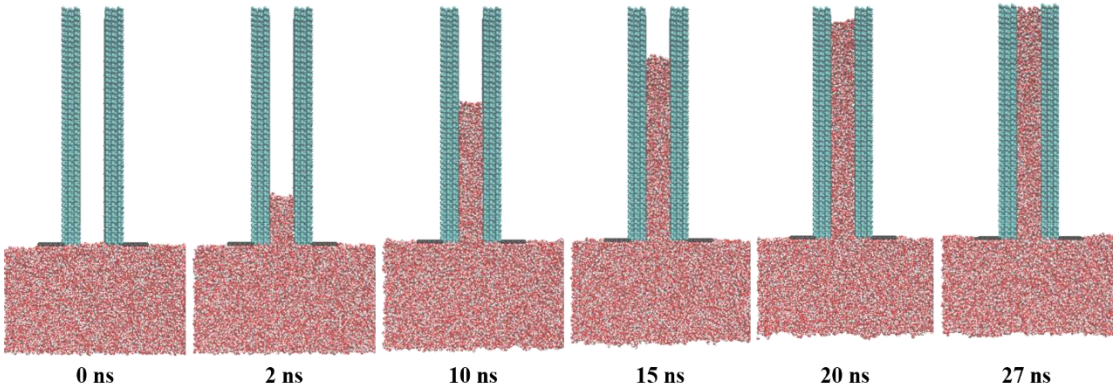

Figure 5. Snapshots of the imbibition process of water transport in the phosphorene-based nanochannel with N = 4.

The imbibition dynamics can be analyzed from the square of the penetration length (l^2) versus time and the variation of the imbibition velocity ($v_z = dl/dt$) with the inverse of penetration length ($1/l$). The simulation results for the walls with armchair and zigzag orientations in the channel with a width of N = 2 are presented in **Figure 6(a)**. It is somewhat surprising to find that the orientation of the phosphorene wall affects the imbibition dynamics, which still follows the typical relation $l^2 = \alpha t$. The capillary flow stops at the end of the channel after 20 ns for the armchair orientation but it halts after 15

doi:10.6342/NTU202301104

ns for the zigzag orientation. This result indicates that the capillary flow is faster in the zigzag orientation than in the armchair orientation. In fact, as shown in the inset, the imbibition velocity (v_z) is consistently faster in the zigzag orientation than in the armchair orientation at the same position of the meniscus. The ratio of the slope (α) associated with the zigzag orientation to that associated with the armchair orientation is approximately equal to 1.2.

According to **Figure 3(b)**, the wetting (spreading) process can be traced by following the change of the internal energy. To differentiate the impact of wall orientation on the imbibition process, the evolution of the internal energy is monitored. **Figure 6(b)** displays the relationship between ΔE and $t^{1/2}$ during the imbibition process for N = 2. As anticipated, the internal energy decreases as the wetted area increases due to imbibition, resulting in $\Delta E(t) < 0$ with $\Delta E(t = 0) = 0$. Since the variation of the penetration length with time follows $l \sim t^{1/2}$, the growth of the wetted area with time must also follow $l \sim t^{1/2}$ during the imbibition process. Therefore, a linear line is observed in the plot of ΔE against $t^{1/2}$. However, when comparing the two orientations (zigzag and armchair), it is found that the slope of the zigzag orientation is steeper than that of the armchair orientation. Note that at the end of the imbibition process, the values of ΔE for both orientations are similar, with an approximate value of $\Delta E \sim -0.031$ kcal/mol. This is simply because filling out the nanochannel yields the same equilibrium wetted area for both orientations of walls. The difference in slope between the two orientations can be attributed to different imbibition rates. Since the imbibition rate of the zigzag orientation is faster than that of the armchair orientation (see **Figure 6(a)**), the internal energy decreases more rapidly for the former than the latter (see **Figure 6(b)**).

doi:10.6342/NTU202301104

(a)

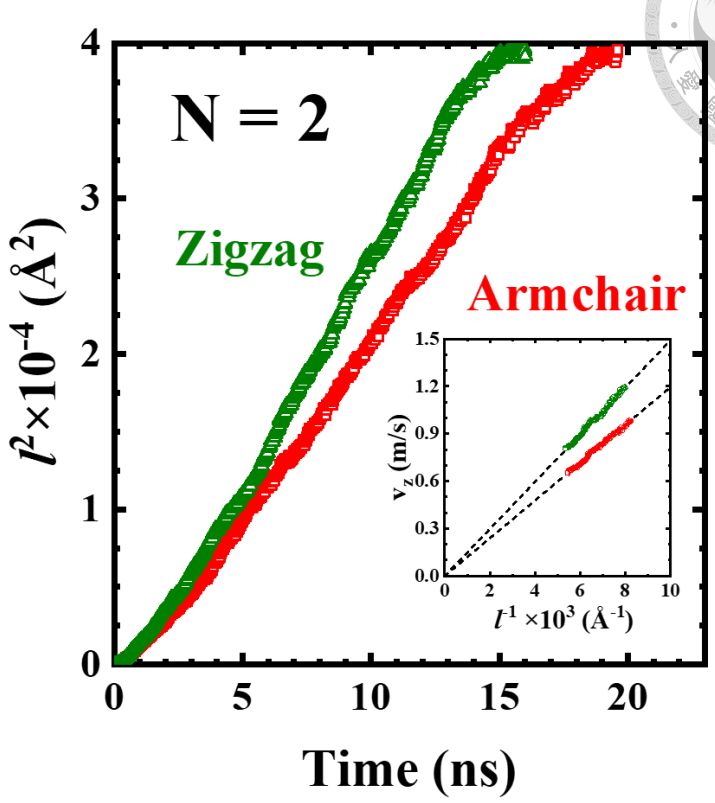

(b)

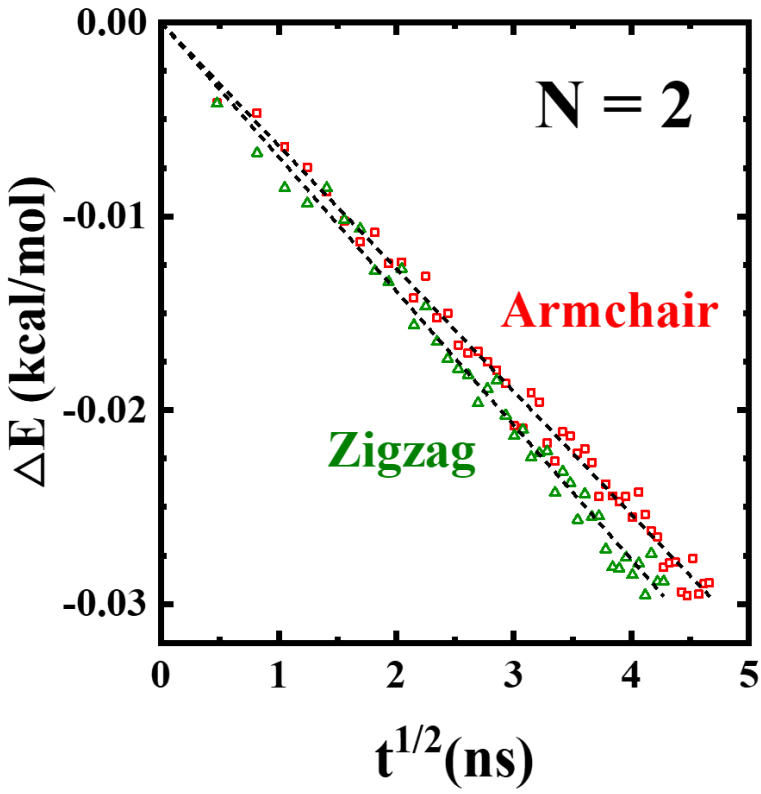

doi:10.6342/NTU202301104

Figure 6. (a) The square of the penetration length (l^2) is plotted against time for both orientations of walls with the channel width N = 2. The inset demonstrates the variation of the imbibition velocity (v_z) with the inverse of the penetration length. (b) The variation of the change in internal energy with the square root of time.

The difference in imbibition rate between the two orientations is noticeable for channel widths of N = 2 to 5, but the difference becomes less pronounced as N increases. As the channel width is sufficiently large (N ≥ 6), the impact of wall orientation on the imbibition process becomes insignificant. **Figure 7(a)** shows the plot of l^2 against time for the two orientations of the phosphorene nanochannel with N = 8. It can be observed that the imbibition dynamics for both orientations are essentially the same, and the capillary flows for both orientations reach the end of the channel at about 36 ns. **Figure 7(b)** shows the variation of ΔE with $t^{1/2}$ for the two orientations, and their data points cannot be distinguished from one another. The results of the penetration length and the change in internal energy are consistent with each other, indicating no impact of wall orientation on the imbibition process for N = 8. The aforementioned analyses indicate that the influence of wall orientation on the imbibition dynamics is significant only in phosphorene nanochannel with smaller widths. This observation is consistent with our general understanding that the surface characteristics of the wall affect laminar fluid flow when the surface roughness is comparable to the channel width [72-74]. The capillary flowrate depends on the competition between the driving force associated with surface wettability and the frictional resistance to fluid flow. For small phosphorene-based nanochannels, the surface wettability in terms of the contact angle is found to be insensitive to the two wall orientations (see Sec. 3.1), suggesting the same driving forces. In contrast, the frictional resistance to the flow along the groove (zigzag orientation) may be weaker than that against periodic protrusions (armchair orientation). Consequently, the

doi:10.6342/NTU202301104

imbibition process of the zigzag orientation is faster than that of the armchair orientation for narrower channels but the differences vanish for sufficiently large channels.

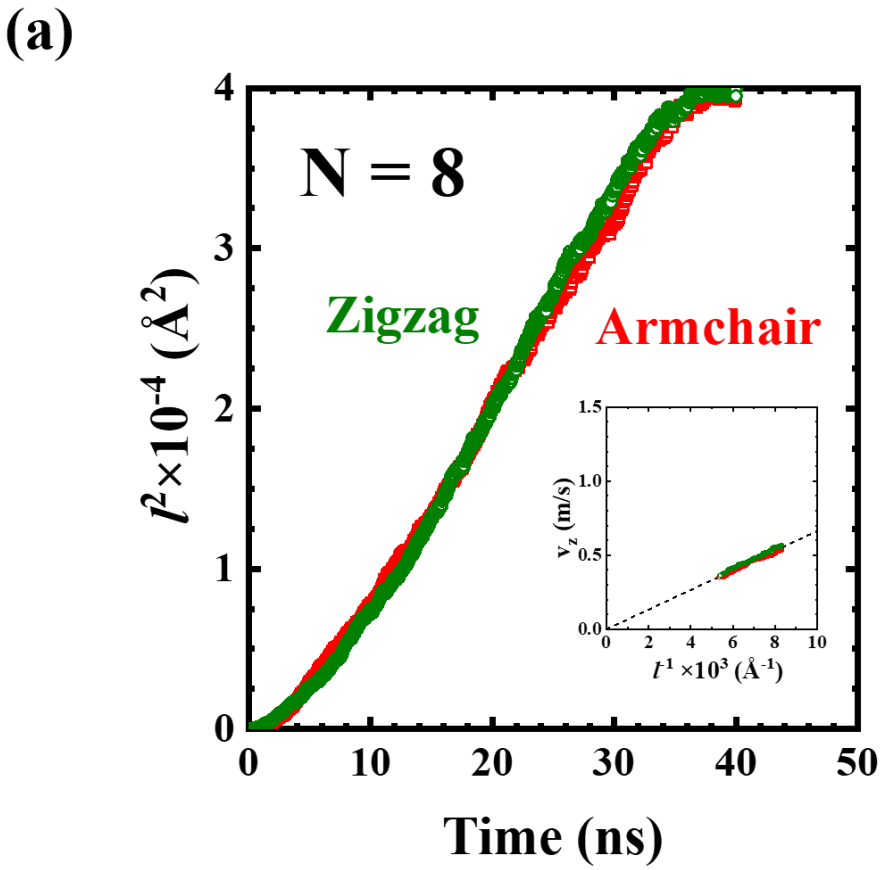

doi:10.6342/NTU202301104

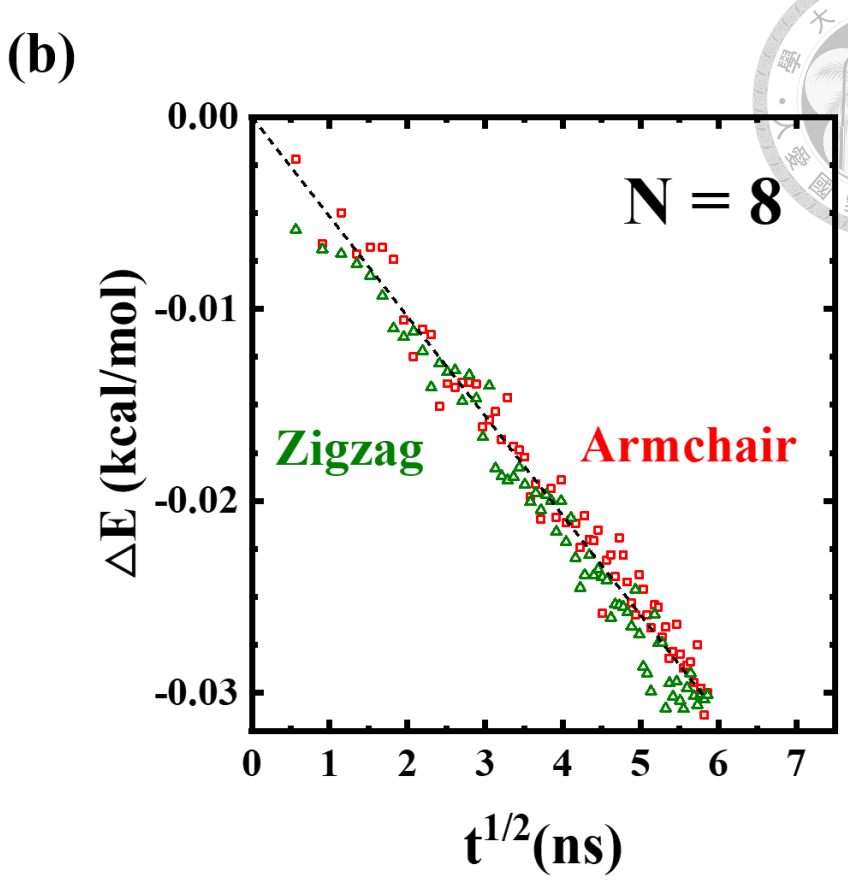

Figure 7. (a) The square of the penetration length (l^2) is plotted against time for both orientations of walls with the channel width N = 8. The inset demonstrates the variation of the imbibition velocity (v_z) with the inverse of the penetration length. (b) The variation of the change in internal energy with the square root of time.

3.3 Effect of channel width and comparison with graphene nanochannels

The imbibition rate is known to depend highly on the channel width based on experimental results [24, 26] and Washburn's equation [28]. Therefore, the spontaneous imbibition process of water in phosphorene nanochannels is studied for different channel widths. **Figure 8(a)** shows how l^2 changes over time for the nanoslit with N = 3, 5, and 8 (zigzag orientation), where one can observe that the relationship $l^2 = \alpha t$ holds true. Furthermore, one can find that the imbibition velocity is inversely proportional to l^{-1} and

doi:10.6342/NTU202301104

follows the relationship $v_z = dl/dt = \alpha/(2l)$, as demonstrated in the inset. Evidently, the imbibition rate, represented by the slope α, is found to decrease with increasing channel width. According to Washburn's equation with no-slip boundary condition ($l_s = 0$), the slope is related to the channel width as $\alpha = \gamma_{lv}\cos(\theta_D)w/(3\mu)$. This expression suggests that the imbibition rate is linearly proportional to the channel width. However, our simulation results for both wall orientations contradict the expected behavior predicted by Washburn's equation. This consequence suggests that Washburn's equation is inadequate in accurately capturing the imbibition dynamics in phosphorene nanochannels.

In addition to the penetration length, the imbibition dynamics can also be analyzed by examining the evolution of the internal energy resulting from wetting. **Figure 8(b)** illustrates the change of ΔE with $t^{1/2}$ for channel widths of N = 3, 5, and 8. The internal energy always decreases over time and becomes constant as the meniscus reaches the end of the channel. Consistent with the evolution of the penetration length, the decay of the internal energy is slower for wider channel widths. As previously discussed (see Sec. 3.2), ΔE(t) is proportional to l(t) due to the increase in the wetted area. This result once again verifies that the effect of the channel width on the imbibition rate is opposite to the prediction by Washburn's equation. In Washburn's model, the relationship between imbibition velocity and channel width can be explained by the balance between the driving force (Laplace pressure), which is proportional to γ_{lv}/w, and the resistive force, which is proportional to $\mu v_z/w^2$ [75]. The inability of Washburn's model to accurately describe the imbibition dynamics in phosphorene nanochannels may be attributed to the inaccuracy associated with the frictional force, since the validity of Laplace pressure has been confirmed in Sec. 3.1.

doi:10.6342/NTU202301104

(a)

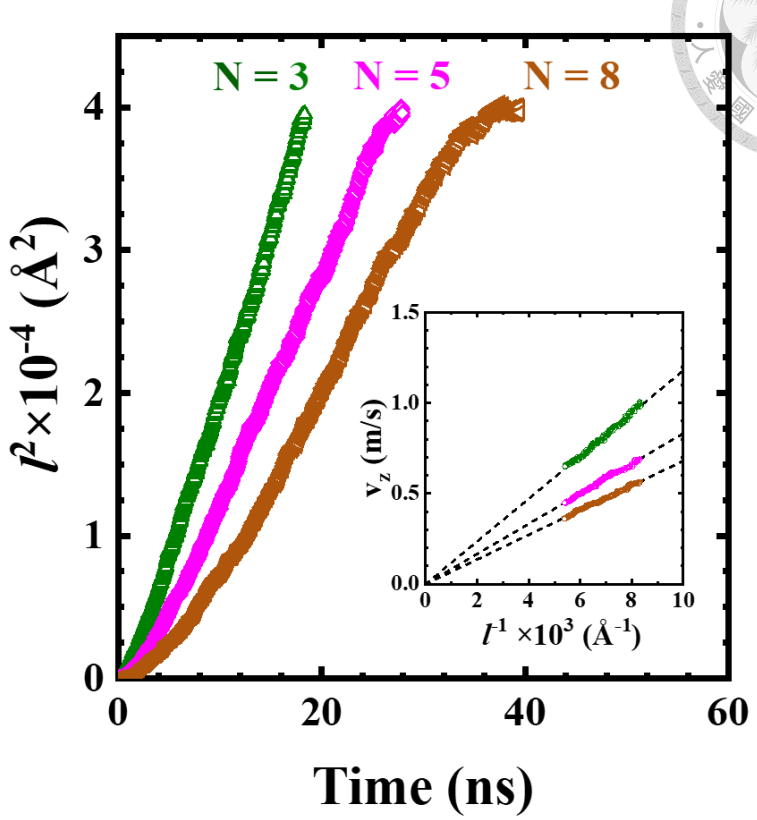

(b)

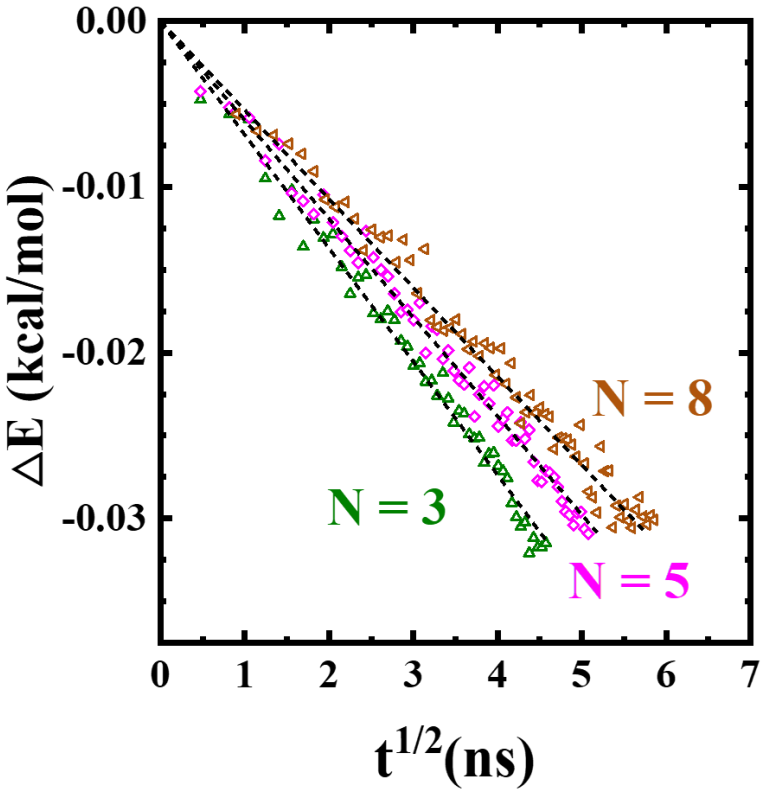

doi:10.6342/NTU202301104

Figure 8. (a) The square of the penetration length is plotted against time for channel widths N = 3, 5, and 8 with the zigzag orientation. The inset demonstrates the variation of the imbibition velocity with l^{-1}. (b) The variation of internal energy (ΔE) with the square root of time for different channel widths.

As the width of the nanochannel decreases to N = 1 (w = 0.52 nm), the imbibition velocity is expected to be the fastest and dependent on the wall orientation, as inferred from the interpolation of previous results. Contrary to expectations, the imbibition rate of N = 1 is surprisingly found to be the slowest among all our simulations. Furthermore, it is independent of the zigzag and armchair orientations. **Figure 9(a)** shows the variations of the penetration length (l) and ΔE with $t^{1/2}$ for the channel width N = 1. The imbibition process took approximately 69 ns to reach the end of the channel with N = 1 for both orientations, while it only took 40 ns for N = 8. The abnormal behavior is also evident in the evolution of internal energy, as illustrated in **Figure 9(a)**. Despite having the same wetted area as the other channel widths, it is observed that the lowest value of ΔE for N = 1 is approximately -0.06 kcal/mol, which is significantly lower than the value of -0.031 kcal/mol observed for other channel widths. The peculiarity associated with N = 1 can be realized from the comparable size between the water molecule (0.3 nm) and the channel width (0.52 nm). Obviously, in the nanoslit, only a maximum of two layers of water molecules can fit, rendering the continuum assumption potentially invalid. **Figure 9(b)** shows the density distribution of water in the channel with N = 1 and 2. Four peaks can be identified in ρ(x) for N = 2. The peaks near the wall, with a density of 2420 kg/m^3, are significantly higher than the peaks in the middle, which have a density close to the bulk density of 997 kg/m^3. In contrast, for N = 1, two prominent peaks near the wall exhibit a density of 3923 kg/m^3, which is significantly higher than the density of the peaks near the wall observed for N = 2. The two minor peaks in the middle, with a density much lower

doi:10.6342/NTU202301104

than the bulk value, do not indicate the presence of distinct water layers. The anomaly associated with N = 1 can be attributed to the extremely high local density of water near the phosphorene wall, leading to significantly increased liquid-solid interactions and friction. The higher liquid-solid interaction results in a lower value of ΔE, while the greater liquid-solid friction causes a high resistance to capillary flow and a lower imbibition rate.

(a)

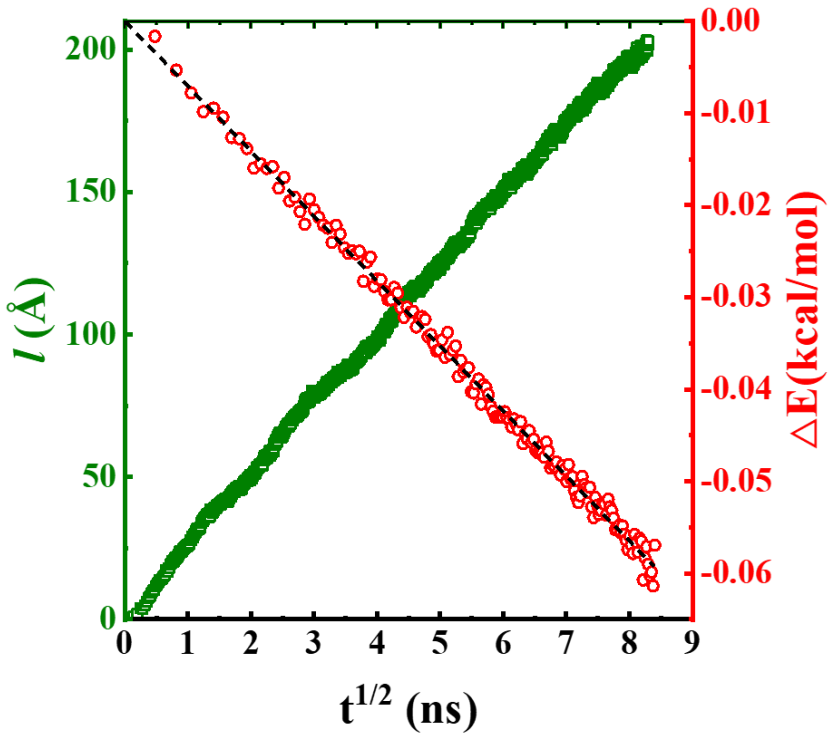

doi:10.6342/NTU202301104

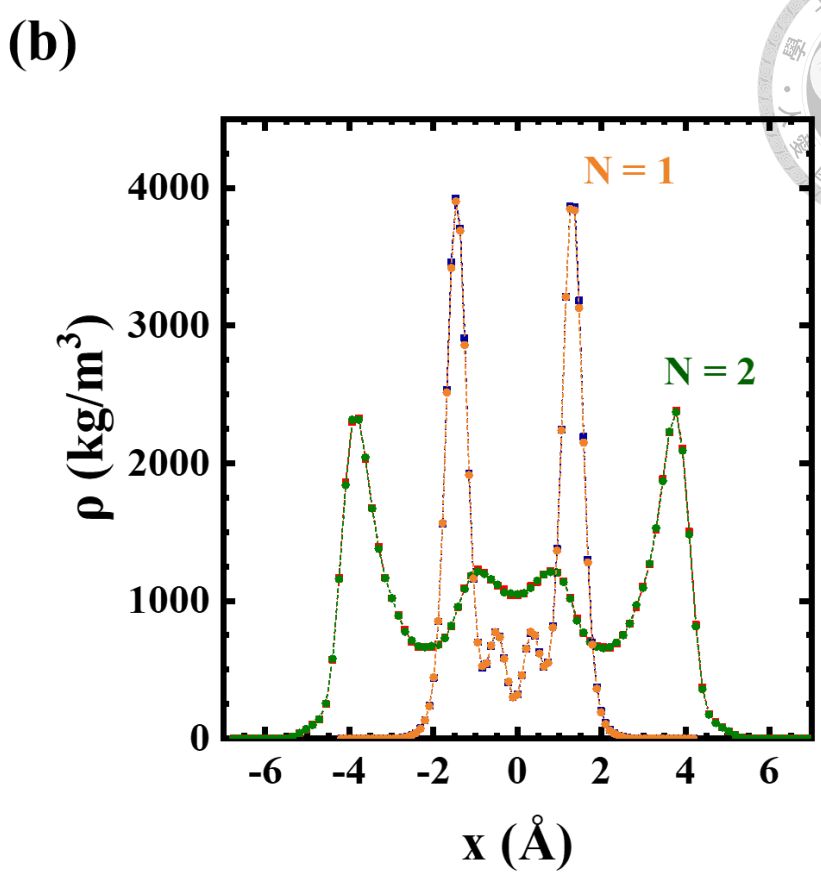

Figure 9. (a) The penetration length and internal energy are plotted against $t^{1/2}$ for the channel width N = 1 with the zigzag orientation. (b) The density distribution of water in the phosphorene nanochannel for N =1 and 2.

In contrast to smooth graphene-based nanochannels, phosphorene-based nanochannels exhibit molecular-level roughness on the walls. While surface roughness on channel walls does not have an impact on laminar flow in large channel widths, it has been reported to influence the flow behavior in nanoscale channels [76]. Consequently, the behavior of water transport in graphene-based and phosphorene-based nanoslits is expected to differ at the same channel width. As illustrated in **Figure 10**, a comparison is made between graphene-based and phosphorene-based nanoslits based on the imbibition velocity (v_z) and the flow rate per unit length ($Q = v_z w$) at the position z = 19 nm, which are obtained from simulations. **Figure 10(a)** shows that the imbibition velocity of both

doi:10.6342/NTU202301104

graphene and phosphorene nanoslits decreases monotonically as the channel width increases from w = 0.3 to 4.2 nm, except for the phosphorene channel with N = 1. Indeed, this result of the channel width-dependence contradicts the prediction of Washburn's equation. It is evident that the imbibition velocities of water in the graphene-based channels are always significantly higher than those in the phosphorene-based channels, regardless of the channel width. Note that the driving force of capillary flow based on surface wettability (contact angle) is slightly larger for the phosphorene surface ($\theta_c \sim 68.2°$) compared to the graphene surface ($\theta_c \sim 75.9°$). Therefore, the capillary flow is primarily governed by the resistance of wall friction, which is influenced by surface roughness. **Figure 10(b)** depicts the variation of the flow rate (Q) with the channel width (w) for both types of nanoslits at the position z = 19 nm. While Q increases monotonically with higher w for phosphorene nanoslits, it exhibits a non-monotonic behavior for graphene nanoslits. As anticipated, the flow rates in graphene nanoslits are consistently higher than those in phosphorene nanoslits for the same channel width. The difference in imbibition velocity between the two types of channels decrease as the channel width increases. This observation suggests that the effect of surface roughness becomes less noticeable with increasing the channel width, but it remains significant in nanoscale channels.

doi:10.6342/NTU202301104

(a)

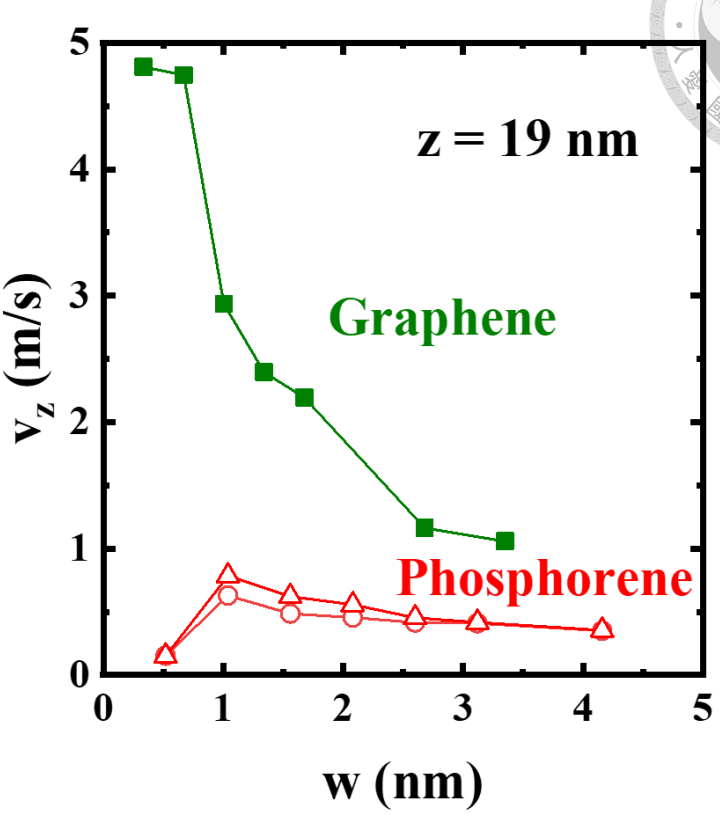

(b)

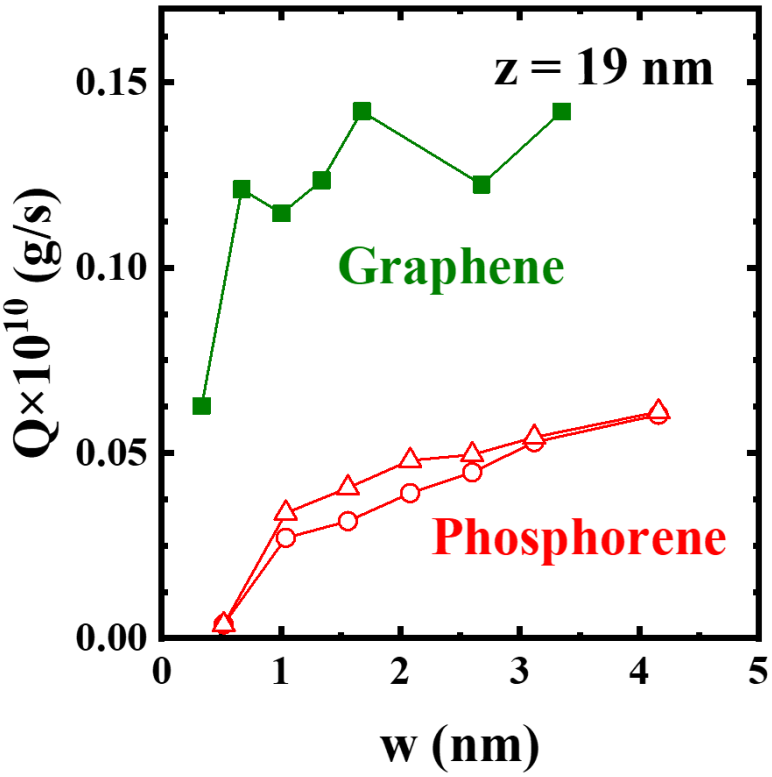

doi:10.6342/NTU202301104

Figure 10. The variation of (a) the imbibition velocity (v_z) and (b) the flow rate (Q) of water with the channel width (w) for both graphene- and phosphorene-based nanoslits at z = 19 nm.

4. Conclusion

The wetting behavior of water nanodroplets on a phosphorene sheet and the imbibition dynamics of water in phosphorene nanoslits were explored by MD. The spreading dynamics beyond the inertial timescale, based on the wetted area, were observed to approximately follow a power law relationship, $A \sim t^{1/2}$, where the exponent (1/2) falls between that of inertial spreading (1) and Tanner's law (1/5). The decrease in internal energy, accompanying the increase in the wetted area, was also observed to follow $\Delta E \sim -t^{1/2}$. The deviation of the spreading process from Tanner's law is likely attributed to a large contact angle and a finite time to reach equilibrium. Additionally, water plugs confined within nanoslits were examined, and both equilibrium contact angle and Laplace pressure were determined. The equilibrium contact angle was measured to be around 70°, consistent with previous studies, and the applicability of the Young-Laplace equation at the nanoscale was verified.

In the imbibition process, the dynamics of the penetration length and the change in internal energy were found to be consistent with each other, both exhibiting a proportionality to $t^{1/2}$. It was observed that the imbibition rate in narrow nanoslits (N = 2 ~ 5) is dependent on the orientation of the phosphorene wall. It is faster in the zigzag orientation compared to the armchair orientation. Nonetheless, the influence of wall orientations gradually diminishes as the channel width increases. This finding may be explained by the understanding that when the surface roughness is comparable to the channel width, the frictional resistance to laminar flow along the groove is weaker compared to the resistance caused by periodic protrusions. Except for N = 1, it was

doi:10.6342/NTU202301104

observed that the imbibition rate decreases with increasing channel width (N), which contradicts the prediction of Washburn's equation. This discrepancy may be attributed to the inaccuracy of Washburn's equation in accounting for the frictional force. The imbibition velocity in graphene-based channels is consistently higher than that in phosphorene-based channels. However, the difference between them diminishes as the channel width increases, suggesting that the impact of surface roughness becomes less pronounced with larger channel widths.

Reference

1. Woodstock, L., *Seed imbibition: a critical period for successful germination.* Journal of Seed Technology, 1988: p. 1-15.
2. Cai, J. and B. Yu, *A discussion of the effect of tortuosity on the capillary imbibition in porous media.* Transport in porous media, 2011. **89**(2): p. 251-263.
3. Wu, P., A. Nikolov, and D. Wasan, *Capillary dynamics driven by molecular self-layering.* Advances in colloid and interface science, 2017. **243**: p. 114-120.
4. Zhmud, B., F. Tiberg, and K. Hallstensson, *Dynamics of capillary rise.* Journal of colloid and interface science, 2000. **228**(2): p. 263-269.
5. Hampton, M.A. and A.V. Nguyen, *Nanobubbles and the nanobubble bridging capillary force.* Advances in colloid and interface science, 2010. **154**(1-2): p. 30-55.
6. Ajeel, R.K., K. Sopian, and R. Zulkifli, *Thermal-hydraulic performance and design parameters in a curved-corrugated channel with L-shaped baffles and nanofluid.* Journal of Energy Storage, 2021. **34**: p. 101996.
7. Park, H.G. and Y. Jung, *Carbon nanofluidics of rapid water transport for energy applications.* Chemical Society Reviews, 2014. **43**(2): p. 565-576.

doi:10.6342/NTU202301104

8. Joshi, R., et al., *Precise and ultrafast molecular sieving through graphene oxide membranes.* science, 2014. **343**(6172): p. 752-754.

9. Cai, J., et al., *Capillary imbibition and flow of wetting liquid in irregular capillaries: A 100-year review.* Advances in Colloid and Interface Science, 2022: p. 102654.

10. Washburn, E.W., *The dynamics of capillary flow.* Physical review, 1921. **17**(3): p. 273.

11. Andredaki, M., A. Georgoulas, and M. Marengo, *Numerical investigation of quasi-sessile droplet absorption into wound dressing capillaries.* Physics of Fluids, 2020. **32**(9): p. 092112.

12. Fries, N. and M. Dreyer, *An analytic solution of capillary rise restrained by gravity.* Journal of colloid and interface science, 2008. **320**(1): p. 259-263.

13. Behroozi, F., *A Fresh Look at the Young-Laplace Equation and Its Many Applications in Hydrostatics.* The Physics Teacher, 2022. **60**(5): p. 358-361.

14. Fries, N., *Capillary transport processes in porous materials-experiment and model*. 2010: Cuvillier Verlag.

15. Li, K. and H. Zhao, *Fractal prediction model of spontaneous imbibition rate.* Transport in porous media, 2012. **91**: p. 363-376.

16. Li, K., et al., *Criteria for applying the Lucas-Washburn law.* Scientific reports, 2015. **5**(1): p. 14085.

17. Siebold, A., et al., *Effect of dynamic contact angle on capillary rise phenomena.* Colloids and surfaces A: Physicochemical and engineering aspects, 2000. **161**(1): p. 81-87.

18. Bocquet, L., *Nanofluidics coming of age.* Nature materials, 2020. **19**(3): p. 254-256.

doi:10.6342/NTU202301104

19. Mailly, D., *Nanofabrication techniques.* The European Physical Journal Special Topics, 2009. **172**(1): p. 333-342.

20. Stepanova, M. and S. Dew, *Nanofabrication: techniques and principles*. 2011: Springer Science & Business Media.

21. Biswas, A., et al., *Advances in top–down and bottom–up surface nanofabrication: Techniques, applications & future prospects.* Advances in colloid and interface science, 2012. **170**(1-2): p. 2-27.

22. Williams, C.D., et al., *A molecular simulation study into the stability of hydrated graphene nanochannels used in nanofluidics devices.* Nanoscale, 2022. **14**(9): p. 3467-3479.

23. Geim, A.K. and I.V. Grigorieva, *Van der Waals heterostructures.* Nature, 2013. **499**(7459): p. 419-425.

24. Radha, B., et al., *Molecular transport through capillaries made with atomic-scale precision.* Nature, 2016. **538**(7624): p. 222-225.

25. Xie, Q., et al., *Ion transport in graphene nanofluidic channels.* Nanoscale, 2016. **8**(47): p. 19527-19535.

26. Holt, J.K., et al., *Fast mass transport through sub-2-nanometer carbon nanotubes.* Science, 2006. **312**(5776): p. 1034-1037.

27. Majumder, M., et al., *Enhanced flow in carbon nanotubes.* Nature, 2005. **438**(7064): p. 44-44.

28. Wang, T.-Y., et al., *Anomalous spontaneous capillary flow of water through graphene nanoslits: Channel width-dependent density.* Journal of Molecular Liquids, 2022. **352**: p. 118701.

29. Jaeger, F., O.K. Matar, and E.A. Müller, *Transport properties of water confined in a graphene nanochannel.* arXiv preprint arXiv:1901.06865, 2019.

doi:10.6342/NTU202301104

30. Zhang, W., et al., *Revealing the importance of surface morphology of nanomaterials to biological responses: Adsorption of the villin headpiece onto graphene and phosphorene.* Carbon, 2015. **94**: p. 895-902.

31. Ling, X., et al., *The renaissance of black phosphorus.* Proceedings of the National Academy of Sciences, 2015. **112**(15): p. 4523-4530.

32. Fei, R. and L. Yang, *Strain-engineering the anisotropic electrical conductance of few-layer black phosphorus.* Nano letters, 2014. **14**(5): p. 2884-2889.

33. Sun, Z., et al., *Ultrasmall black phosphorus quantum dots: synthesis and use as photothermal agents.* Angewandte Chemie International Edition, 2015. **54**(39): p. 11526-11530.

34. Liu, H., et al., *Semiconducting black phosphorus: synthesis, transport properties and electronic applications.* Chemical Society Reviews, 2015. **44**(9): p. 2732-2743.

35. Li, L., et al., *Black phosphorus field-effect transistors.* Nature nanotechnology, 2014. **9**(5): p. 372-377.

36. Brown, A. and S. Rundqvist, *Refinement of the crystal structure of black phosphorus.* Acta Crystallographica, 1965. **19**(4): p. 684-685.

37. Cartz, L., et al., *Effect of pressure on bonding in black phosphorus.* The Journal of Chemical Physics, 1979. **71**(4): p. 1718-1721.

38. Cai, Y., G. Zhang, and Y.-W. Zhang, *Electronic properties of phosphorene/graphene and phosphorene/hexagonal boron nitride heterostructures.* The Journal of Physical Chemistry C, 2015. **119**(24): p. 13929-13936.

39. Qiao, J., et al., *High-mobility transport anisotropy and linear dichroism in few-layer black phosphorus.* Nature communications, 2014. **5**(1): p. 4475.

doi:10.6342/NTU202301104

40. Rabiei Baboukani, A., et al., *Liquid-Based Exfoliation of Black Phosphorus into Phosphorene and Its Application for Energy Storage Devices.* Small Structures, 2021. **2**(5): p. 2000148.

41. Zhang, Y., et al., *An air-stable densely packed phosphorene–graphene composite toward advanced lithium storage properties.* Advanced Energy Materials, 2016. **6**(12): p. 1600453.

42. Zhang, H., *Ultrathin two-dimensional nanomaterials.* ACS nano, 2015. **9**(10): p. 9451-9469.

43. Ambrosi, A., Z. Sofer, and M. Pumera, *Electrochemical exfoliation of layered black phosphorus into phosphorene.* Angewandte Chemie International Edition, 2017. **56**(35): p. 10443-10445.

44. Xiao, H., et al., *Electrochemical cathode exfoliation of bulky black phosphorus into few-layer phosphorene nanosheets.* Electrochemistry Communications, 2018. **89**: p. 10-13.

45. Xing, C., et al., *Preparations, properties and applications of low-dimensional black phosphorus.* Chemical Engineering Journal, 2019. **370**: p. 120-135.

46. Wang, G., et al., *Degradation of phosphorene in air: understanding at atomic level.* 2D Materials, 2016. **3**(2): p. 025011.

47. Huang, Y., et al., *655 J. Decker, W. Ji, RS Ruoff, P. Sutter, Interaction of Black Phosphorus with Oxygen and 656 Water.* Chem. Mater, 2016. **28**: p. 8330-8339.

48. Zhang, W., et al., *Molecular structure and dynamics of water on pristine and strained phosphorene: wetting and diffusion at nanoscale.* Scientific reports, 2016. **6**(1): p. 38327.

49. Choi, J.R., et al., *Black phosphorus and its biomedical applications.* Theranostics, 2018. **8**(4): p. 1005.

doi:10.6342/NTU202301104

50. Lange, S., P. Schmidt, and T. Nilges, *Au3SnP7@ black phosphorus: an easy access to black phosphorus.* Inorganic chemistry, 2007. **46**(10): p. 4028-4035.

51. Humphrey, W., A. Dalke, and K. Schulten, *VMD: visual molecular dynamics.* Journal of molecular graphics, 1996. **14**(1): p. 33-38.

52. Phillips, J.C., et al., *Scalable molecular dynamics with NAMD.* Journal of computational chemistry, 2005. **26**(16): p. 1781-1802.

53. Phillips, J.C., et al., *Scalable molecular dynamics on CPU and GPU architectures with NAMD.* The Journal of chemical physics, 2020. **153**(4): p. 044130.

54. Abascal, J.L. and C. Vega, *A general purpose model for the condensed phases of water: TIP4P/2005.* The Journal of chemical physics, 2005. **123**(23): p. 234505.

55. González, M.A. and J.L. Abascal, *The shear viscosity of rigid water models.* The Journal of chemical physics, 2010. **132**(9): p. 096101.

56. Sresht, V., A.A. Padua, and D. Blankschtein, *Liquid-phase exfoliation of phosphorene: design rules from molecular dynamics simulations.* ACS nano, 2015. **9**(8): p. 8255-8268.

57. Hultgren, R., N. Gingrich, and B. Warren, *The atomic distribution in red and black phosphorus and the crystal structure of black phosphorus.* The Journal of Chemical Physics, 1935. **3**(6): p. 351-355.

58. Liu, X., et al., *Resolving the in-plane anisotropic properties of black phosphorus.* Small Methods, 2017. **1**(6): p. 1700143.

59. Deshmukh, S.A., G. Kamath, and S.K. Sankaranarayanan, *Comparison of the interfacial dynamics of water sandwiched between static and free-standing fully flexible graphene sheets.* Soft Matter, 2014. **10**(23): p. 4067-4083.

60. Foloppe, N. and J. MacKerell, Alexander D, *All-atom empirical force field for nucleic acids: I. Parameter optimization based on small molecule and condensed*

doi:10.6342/NTU202301104

phase macromolecular target data. Journal of computational chemistry, 2000. **21**(2): p. 86-104.

61. Chen, S., et al., *Anisotropic wetting characteristics of water droplets on phosphorene: roles of layer and defect engineering.* The Journal of Physical Chemistry C, 2018. **122**(8): p. 4622-4627.

62. Bird, J.C., S. Mandre, and H.A. Stone, *Short-time dynamics of partial wetting.* Physical review letters, 2008. **100**(23): p. 234501.

63. Winkels, K.G., et al., *Initial spreading of low-viscosity drops on partially wetting surfaces.* Physical Review E, 2012. **85**(5): p. 055301.

64. Chen, L. and E. Bonaccurso, *Effects of surface wettability and liquid viscosity on the dynamic wetting of individual drops.* Physical Review E, 2014. **90**(2): p. 022401.

65. Tanner, L., *The spreading of silicone oil drops on horizontal surfaces.* Journal of Physics D: Applied Physics, 1979. **12**(9): p. 1473.

66. Hu, S.-W., et al., *Peculiar Wetting of N, N-dimethylformamide: Expansion, contraction, and self-running.* The Journal of Physical Chemistry C, 2019. **123**(40): p. 24477-24486.

67. White, L.R., *On deviations from Young's equation.* Journal of the Chemical Society, Faraday Transactions 1: Physical Chemistry in Condensed Phases, 1977. **73**: p. 390-398.

68. Makkonen, L., *Young's equation revisited.* Journal of Physics: Condensed Matter, 2016. **28**(13): p. 135001.

69. Mo, J., et al., *Fluid release pressure for nanochannels: the Young–Laplace equation using the effective contact angle.* Nanoscale, 2019. **11**(17): p. 8408-8415.

70. Chu, K.-C., H.-K. Tsao, and Y.-J. Sheng, *Pressure-gated capillary nanovalves*

doi:10.6342/NTU202301104

based on liquid nanofilms. Journal of colloid and interface science, 2020. **560**: p. 485-491.

71. Lin, C.-M., et al., *Size-dependent properties of small unilamellar vesicles formed by model lipids.* Langmuir, 2012. **28**(1): p. 689-700.

72. Kandlikar, S.G., et al., *Characterization of surface roughness effects on pressure drop in single-phase flow in minichannels.* Physics of Fluids, 2005. **17**(10): p. 100606.

73. Zhou, G. and S.-C. Yao, *Effect of surface roughness on laminar liquid flow in micro-channels.* Applied Thermal Engineering, 2011. **31**(2-3): p. 228-234.

74. Taylor, J.B., A.L. Carrano, and S.G. Kandlikar, *Characterization of the effect of surface roughness and texture on fluid flow—past, present, and future.* International journal of thermal sciences, 2006. **45**(10): p. 962-968.

75. Chu, K.-C., H.-K. Tsao, and Y.-J. Sheng, *Penetration dynamics through nanometer-scale hydrophilic capillaries: Beyond Washburn's equation and extended menisci.* Journal of colloid and interface science, 2019. **538**: p. 340-348.

76. Cheng, Y.-T., et al., *Imbibition dynamics and steady flows in graphene nanochannels with sparse geometric and chemical defects.* Physics of Fluids, 2022. **34**(11): p. 112003.

doi:10.6342/NTU202301104